A&A 634, A9 (2020)
https://doi.org/10.1051/0004-6361/201936867


Astronomy & Astrophysics

# The flickering nuclear activity of Fornax A★

F. M. Maccagni[1], M. Murgia[1], P. Serra[1], F. Govoni[1], K. Morokuma-Matsui[2], D. Kleiner[1], S. Buchner[3], G. I. G. Józsa[3,4,5], P. Kamphuis[6], S. Makhathini[4], D. Cs. Molnár[1], D. A. Prokhorov[7], A. Ramaila[3,4], M. Ramatsoku[1,4], K. Thorat[3,4], and O. Smirnov[3,4]

[1] INAF – Osservatorio Astronomico di Cagliari, via della Scienza 5, 09047 Selargius, CA, Italy
e-mail: filippo.maccagni@inaf.it
[2] Institute of Astronomy, Graduate School of Science, The University of Tokyo, 2-21-1 Osawa, Mitaka, Tokyo 181-0015, Japan
[3] South African Radio Astronomy Observatory, Black River Park, 2 Fir Street, Observatory, Cape Town 7925, South Africa
[4] Department of Physics and Electronics, Rhodes University, PO Box 94, Makhanda 6140, South Africa
[5] Argelander-Institut für Astronomie, Auf dem Hügel 71, 53121 Bonn, Germany
[6] Ruhr-University Bochum, Faculty of Physics and Astronomy, Astronomical Institute, 44780 Bochum, Germany
[7] School of Physics, University of the Witwatersrand, Private Bag 3, 2050 Johannesburg, South Africa

Received 7 October 2019 / Accepted 20 November 2019

**ABSTRACT**

We present new observations of Fornax A taken at ∼1 GHz with the MeerKAT telescope and at ∼6 GHz with the Sardinia Radio Telescope (SRT). The sensitive (noise ∼16 $\mu$Jy beam$^{-1}$), high-resolution ($\lesssim$10″) MeerKAT images show that the lobes of Fornax A have a double-shell morphology, where dense filaments are embedded in a diffuse and extended cocoon. We study the spectral properties of these components by combining the MeerKAT and SRT observations with archival data between 84 MHz and 217 GHz. For the first time, we show that multiple episodes of nuclear activity must have formed the extended radio lobes. The modelling of the radio spectrum suggests that the last episode of injection of relativistic particles into the lobes started ∼24 Myr ago and stopped 12 Myr ago. More recently (∼3 Myr ago), a less powerful and short ($\lesssim$1 Myr) phase of nuclear activity generated the central jets. Currently, the core may be in a new active phase. It appears that Fornax A is rapidly flickering. The dense environment around Fornax A has lead to a complex recent merger history for this galaxy, including mergers spanning a range of gas contents and mass ratios, as shown by the analysis of the galaxy's stellar- and cold-gas phases. This complex recent history may be the cause of the rapid, recurrent nuclear activity of Fornax A.

**Key words.** galaxies: individual: Fornax A – galaxies: individual: NGC 1316 – galaxies: active – radio continuum: galaxies – galaxies: jets – radiation mechanisms: non-thermal

## 1. Introduction

Active galactic nuclei (AGNs) are associated with the accretion of material onto a super-massive black hole (SMBH) at the centre of their host galaxy. The energy released by the AGN into the surrounding interstellar medium (ISM) through radiation and/or relativistic jets of radio plasma can drastically change the fate of its host galaxy by removing or displacing the gas in the galaxy and preventing it from cooling to form new stars (see, for example, Fabian 2012; McNamara & Nulsen 2012; Bolatto et al. 2013; Fluetsch et al. 2019). This mechanism, commonly referred to as "AGN feedback", likely plays a fundamental role in regulating the star formation of the host galaxy as well as the observed relation between the masses of the bulge and of the SMBH (e.g. Bower et al. 2006; Croton et al. 2006; Booth & Schaye 2009). Numerical simulations of galaxy evolution indicate that only multiple phases of nuclear activity may prevent the hot circumgalactic gas from cooling back onto the galaxy, and therefore explain the rapid quenching of star formation in early-type galaxies (Ciotti et al. 2010; Ciotti & Ziaee Lorzad 2018). The timescale of the different phases of activity may depend on the environment (Hogan et al. 2015).

Different observations of AGNs at optical and radio wavelengths have suggested that the phase of accretion onto the SMBH, namely the active phase, is short compared to the lifetime of the galaxy, and that it may be recurrent (e.g. Woltjer 1959; Marconi et al. 2004; Saikia & Jamrozy 2009; Shabala et al. 2017; Kuźmicz et al. 2017; Morganti 2017). In the optical bands, the multiple episodes of nuclear activity are sometimes identified by the presence of "light echoes", that is clouds of gas ionised by an AGN in the outskirts of a galaxy without an active core (see, for example, Lintott et al. 2009; Józsa et al. 2009; Comerford et al. 2017). In the radio band, multiple phases of activity can be identified by the presence of both a flat-spectrum core, indicating a recent activity, and large-scale diffuse emission around the AGN, with a steep-spectrum brightening at low frequencies ($\lesssim$1 GHz), tracing the remnants of past activity (Jamrozy et al. 2004; Parma et al. 2007; Shulevski et al. 2012; Brienza et al. 2016). In some cases, jets related to the nuclear activity of the present epoch may also be found (e.g. Jones & Preston 2001; Saikia & Jamrozy 2009; Shulevski et al. 2012).

The radio emission of AGNs allows us to measure the duty cycle of the nuclear activity. In particular, the steepening of the radio spectrum is often interpreted as radiative ageing of the electron population in the relativistic plasma (see,

★ A copy of all the images is available at the CDS via anonymous ftp to cdsarc.u-strasbg.fr (130.79.128.5) or via http://cdsarc.u-strasbg.fr/viz-bin/cat/J/A+A/634/A9 e.g. Carilli et al. 1991; Komissarov & Gubanov 1994; Parma et al. 1999; Murgia et al. 1999, 2011, 2012; Orrù et al. 2010; Harwood et al. 2013; Kolokythas et al. 2015).

In nearby AGNs, different studies have traced the history of injection of relativistic particles from the SMBH into the radio jets and lobes through the pixel-by-pixel study of the spectral index and break-frequency maps of the AGN radio spectrum (e.g. Murgia et al. 2010a,b; Orrù et al. 2010; de Gasperin et al. 2012). In particular, these studies related the energetic output of each episode of AGN activity to the fate of the host galaxy and its surrounding environment (Gizani & Leahy 2003; Stanghellini et al. 2005; de Gasperin et al. 2014; Brienza et al. 2018).

In this paper, we study the radio spectrum of Fornax A, the third brightest nearby radio galaxy ($D_L = 20.8 \pm 0.5$ Mpc; Cantiello et al. 2013)[1] after Centaurus A and M 87, to determine the timescale and the duty cycle of its nuclear activity.

Fornax A is one of the most fascinating radio sources in the local Universe because of its filamentary extended radio lobes (∼1.1° Ekers et al. 1983; Fomalont et al. 1989; Bernardi et al. 2013). To the south of the galaxy, a "bridge" of synchrotron emission connects the two lobes. In the centre, two radio jets are embedded in the host galaxy ($r \lesssim 6$ kpc) and exhibit an s-shaped morphology (Geldzahler & Fomalont 1978, 1984). The emission of the jets extends all the way to the centre of the galaxy at angular resolutions $\gtrsim 1''$ (Geldzahler & Fomalont 1984). Most of the radio emission is produced in the extended lobes. At 1.4 GHz, their total flux density is 121 Jy while that of the jets (including the galaxy centre) is ∼300 mJy (Fomalont et al. 1989). The very central flux density is ∼100 mJy and ∼30 mJy at 1.4 GHz and 4.8 GHz, respectively (at the resolution of $\sim 1''$) while it is ∼7 mJy at 15 GHz (resolution $\sim 0.1''$; Geldzahler & Fomalont 1984). However, no central emission is detected at 2.2 GHz and 8.4 GHz down to 3 and 6 mJy (1 sigma upper limits) at a resolution of 90 and 27 mas, respectively (Jones et al. 1994; Slee et al. 1994). A summary of the properties of Fornax A is shown in Table 1.

Fornax A is hosted by the giant early-type galaxy NGC 1316, which is the brightest member of a galaxy group at the outskirts of the Fornax cluster, likely falling into it (Drinkwater et al. 2001). The brightest cluster galaxy NGC 1399 is located ∼4° to the northeast of Fornax A. NGC 1316 shows clear indications of a past major merger event that likely formed the several tails and loops at the outskirts of the stellar body (Schweizer 1980; Grillmair et al. 1999; Mackie & Fabbiano 1998; Carlqvist 2010; Galametz et al. 2012; Duah Asabere et al. 2016). Deep photometric observations indicate that NGC 1316 may be in a later phase of mass assembly, where smaller satellites recursively accrete into the galaxy (Iodice et al. 2017). The major merger event likely brought large amounts of dust, cold molecular gas (Horellou et al. 2001; Roussel et al. 2007; Galametz et al. 2014; Morokuma-Matsui et al. 2019), and neutral hydrogen (Horellou et al. 2001; Serra et al. 2019) into the centre and around the galaxy.

Based on the spread in age of the globular clusters hosted by NGC 1316 the merger is estimated to have occurred 1–3 Gyr ago (Schweizer 1980; Goudfrooij et al. 2001; Sesto et al. 2016, 2018), and it has been suggested to have possibly triggered the nuclear activity of Fornax A (e.g. Ekers et al. 1983; Fomalont et al. 1989; McKinley et al. 2015). Nevertheless, large uncertainties remain on the timescale of formation of the radio lobes. Moreover, this past merger event does not properly explain the properties of the central emission (Geldzahler & Fomalont 1978, 1984), nor the soft X-ray cavities between the lobes and the host galaxy (Lanz et al. 2010).

**Table 1.** General properties of Fornax A.

| Parameter | Value | Ref. |
|---|---|---|
| Right ascension $\alpha$ (J2000) | $03^{h}22^{m}41.7^{s}$ | (*) |
| Declination $\delta$ (J2000) | $-37^{d}12^{m}30^{s}$ | (*) |
| $D_L$ | 20.8 Mpc | (1) |
| $S_{1.4\,GHz}$ (total) | 128 Jy | (*) |
| $S_{1.4\,GHz}$ (peak) | 105 mJy | (*) |
| $P_{1.4\,GHz}$ (lobes) | $1 \times 10^{25}$ W Hz$^{-1}$ | (*) |
| $P_{1.4\,GHz}$ (peak) | $5.5 \times 10^{22}$ W Hz$^{-1}$ | (*) |
| Lobes radius | $20'$–$28'$ (122–170 kpc) | (*) |
| $B_{eq}$ (Lobes $r < 170$ kpc) | 3.0 $\mu$G | (*) |
| Magnetic field, $B_{av}$ | $2.6 \pm 0.3$ $\mu$G | (2,3) |
| IC magnetic field, $B_{IC}$ | 3.2 $\mu$G | (3) |
| $B/B_{IC}$ | 0.8 | (3) |

**References.** (*) This work (1) Cantiello et al. (2013) (2) Anderson et al. (2018) (3) McKinley et al. (2015).

Crucial information on the pressure of the medium through which the radio lobes are expanding could be provided by high-energy observations, but the extent of the radio lobes of Fornax A and their proximity does not allow a complete mapping of the X-ray halo surrounding the radio source. Nevertheless, some regions of the west lobe of Fornax A are bright at high energies showing $\gamma$-ray emission (Ackermann et al. 2016). The soft X-ray spectrum of the west lobe shows hints of diffuse thermal emission that may trace material entrained by the expanding radio lobes (Seta et al. 2013), which may also explain the presence of the low-polarisation patches in the filaments of the lobes (Anderson et al. 2018). Iyomoto et al. (1998) show that the X-ray spectrum of the nucleus of Fornax A suggests that the AGN is currently inactive, while Lanz et al. (2010) identify two X-ray cavities between the host galaxy and the radio lobes. Ultra-high energy cosmic rays have also been possibly associated with Fornax A (Matthews et al. 2019).

McKinley et al. (2015) studied the total flux density of Fornax A in the radio, X-ray, and $\gamma$-ray frequencies, providing information on the energy that must have been injected by the AGN into the surrounding intergalactic medium (IGM). To gain further insight into how the AGN formed the giant radio lobes and the central emission of Fornax A, it is crucial to spatially resolve these components over a broad radio band and trace the differences in their flux density distributions.

In this paper, we present a new MeerKAT (Jonas & MeerKAT Team 2004) interferometric observation of Fornax A in the *L*-band (900–1710 MHz) and a new Sardinia Radio Telescope (SRT, Bolli et al. 2015; Prandoni et al. 2017) single-dish observation in the *C*-band (5800–6700 MHz). We used these observations, along with archival observations from other radio telescopes, to study the main properties of the flux density of Fornax A between 84 MHz and 217 GHz and to understand the mechanisms and timescales of formation of the lobes and of the jets of this AGN. The paper is structured as follows: in the following section we present the data used to study the radio emission of Fornax A. In Sect. 3 we show the radio spectrum of the lobes and of the central emission. Section 4 focuses on the properties of the radio jets

[1] Throughout this paper we use a ΛCDM cosmology, with Hubble constant $H_0 = 70$ km s$^{-1}$ Mpc$^{-1}$ and $\Omega_\Lambda = 0.7$ and $\Omega_M = 0.3$. At the distance of Fornax A the image scale is 101 parsec/arcsec.

**Table 2.** Main properties of the observations.

| Telescope | Frequency [GHz] | Bandwidth [MHz] | Spatial resolution | Image rms [mJy beam$^{-1}$] |
|---|---|---|---|---|
| MWA $^{(\dagger)}$ | 0.084 | 31 | $5.0' \times 4.7'$ | 256 |
| | 0.105 | 31 | $3.6' \times 3.4'$ | 102 |
| | 0.20 | 61 | $2.3' \times 2.2'$ | 28.1 |
| VLA $^{(\dagger)}$ | 0.32 | 26 | $1.5' \times 0.6'$ | 3.18 |
| MeerKAT | 1.03 | 100 | $11.2'' \times 9.1''$ | 0.03 |
| | 1.44 | 120 | $6.8'' \times 5.8''$ | 0.02 |
| VLA $^{(\dagger)}$ | 1.50 | 12 | $14'' \times 14''$ | 0.15 |
| VLA $^{(\star)}$ | 4.86 | 100 | $3.9'' \times 3.9''$ | 0.08 |
| SRT $^{(\dagger)}$ | 5.80 | 100 | $3.3' \times 3.3'$ | 7.19 |
| | 5.90 | 200 | $3.2' \times 3.2'$ | 7.71 |
| | 6.10 | 200 | $3.1' \times 3.1'$ | 6.79 |
| | 6.30 | 200 | $3.0' \times 3.0'$ | 6.73 |
| | 6.50 | 200 | $2.9' \times 2.9'$ | 6.84 |
| | 6.70 | 200 | $2.8' \times 2.8'$ | 6.95 |
| | 6.87 | 145 | $2.7' \times 2.7'$ | 6.05 |
| VLA $^{(\star)}$ | 14.9 | 100 | $4.1'' \times 4.1''$ | 0.12 |
| *Planck* $^{(\dagger)}$ | 30.0 | 6000 | $32' \times 32'$ | 482 |
| | 40.0 | 4800 | $27' \times 27'$ | 336 |
| | 70.0 | $14\times10^3$ | $13' \times 13'$ | 108 |
| | 100 | $32\times10^3$ | $9.7' \times 9.7'$ | 81.8 |
| ALMA - Morita Array $^{(\star)}$ | 108 | $8 \times 10^3$ | $18.1'' \times 9.0''$ | 0.21 |
| *Planck* $^{(\dagger)}$ | 143 | $46\times10^3$ | $7.2' \times 7.2'$ | 36.9 |
| | 217 | $65\times10^3$ | $5.0' \times 5.0'$ | 26.5 |

**Notes.** $^{(\star)}$Observations considered only for the analysis of the radio emission in the central kiloparsec. $^{(\dagger)}$Observations considered only for the analysis of the radio emission in the east and west lobe.

emission determined from the high-resolution MeerKAT observation. In Sect. 5 we infer the main physical parameters that characterise the flux density of the lobes and central emission. In Sect. 6 we discuss the spectral flux index and break-frequency maps obtained from the MeerKAT images. In Sect. 7 we relate the properties of the radio emission of Fornax A to the nuclear activity that formed it, providing indications on how the extended radio lobes may have expanded in the IGM and suggest a timeline for the nuclear activity. Section 8 presents a summary of the main results of this paper.

## 2. Multi-wavelength observations

The goals of our study are to characterise the AGN activity history that created the large radio lobes and the central emission of Fornax A. The first goal requires, over a wide range of frequencies, images sensitive to low-surface-brightness emission over a wide field of view, since the lobes are faint and extend for $\sim$1° in the sky. To achieve the second goal we need images with $\sim$10″ angular resolution to resolve the central emission.

Over the wide frequency range required to infer the history of the nuclear activity, most available datasets are not suitable for both goals because typically those with a large field of view do not have adequate angular resolution – the only exception being the new MeerKAT data presented here.

For these reasons, we selected two different sets of observations to analyse the radio emission in the lobes and in the centre of Fornax A. To study the lobes we need wide-field-of-view observations sensitive to the diffuse emission of the lobes (i.e. good *uv*-coverage on the short baselines), while arcsecond resolution is not needed. Hence, between 84 and 200 MHz we chose observations from the GaLactic and Extra-galactic All-sky MWA survey (GLEAM; Hurley-Walker et al. 2017) of the Murchinson Wide Field Array. We use the MeerKAT observation to generate images of Fornax A at 1.03 and 1.44 GHz. At 1.5 GHz we chose archival Very Large Array (VLA) observations (Fomalont et al. 1989). Between 5.7 and 6.9 GHz we use the new observation of the SRT. Between 70 GHz and 217 GHz, we selected images of Fornax A from the final release of the *Planck* foreground maps (Planck Collaboration IV 2020).

The second set is needed to study the central emission, and therefore we selected observations with arcsecond resolution: the MeerKAT images at 1.03 and 1.44 GHz, archival VLA observations at 4.8 and 15 GHz (Geldzahler & Fomalont 1984), and an observation at 108 GHz (Morokuma-Matsui et al. 2019) taken with the Morita Array of the Atacama Large Millimeter and submillimeter Array (ALMA).

The main properties of all observations considered in this paper are summarised in Table 2. In the following sections, we provide further details on the new MeerKAT, SRT, and ALMA observations (see Sects. 2.1–2.3, respectively). Details on the reduction of archival observations are given in Appendix A.

### 2.1. MeerKAT: 1.03 GHz and 1.44 GHz

MeerKAT is an interferometric radio telescope built in South Africa as a precursor for the “small dish plus single-pixel, wideband feed” component of the Square Kilometer Array (Jonas & MeerKAT Team 2004; Camilo et al. 2018). In preparation for the MeerKAT Fornax Survey (Serra et al. 2016), whose aim is to study galaxy evolution in the Fornax cluster, we analyse a MeerKAT commissioning observation of Fornax A.

This observation was taken on June 2, 2018, with a reduced array of 40 antennas and the SKARAB-4K correlator (4096 channels with resolution of approximately 209 kHz) over the full MeerKAT bandwidth: 0.86–1.71 GHz. The total observing time on target was 7.8 h.

A complete description of the reduction of this observation can be found in Serra et al. (2019). Here, we focus on how we generated the continuum images of Fornax A between 0.98 and 1.08 GHz and between 1.38 GHz and 1.50 GHz needed for the purposes of this paper.

The reduction of this observation was done with a new pipeline that is being developed for the reduction of continuum and spectral interferometric observations (Makhathini et al. in prep.)[2]. The pipeline is set up in a modular fashion using the platform-independent radio interferometry scripting framework `stimela`[3]. This means that for each step of the data reduction, such as calibration, flagging, and self-calibration, we use tasks from different radio astronomical packages. Imaging was performed in Stokes $I$ using `WSclean` (Offringa et al. 2014). Multi-scale cleaning (Offringa & Smirnov 2017) was performed within a mask marking the regions of Fornax A and of the other sources in the field. In the first imaging step, we generated a clean mask from the VLA observations at 1.5 GHz (Fomalont et al. 1989, see Appendix A). In the subsequent steps, the clean mask was recursively improved by running the source finder `SoFiA` (Serra et al. 2015) on the cleaned image. We iteratively imaged with Briggs weighting `robust=` −0.5, and we calibrated, using `MeqTrees` (Noordam & Smirnov 2010), solving for frequency-independent gain phase with a solution time interval of

[2] https://github.com/ska-sa/meerkathi-public
[3] https://github.com/SpheMakh/Stimela

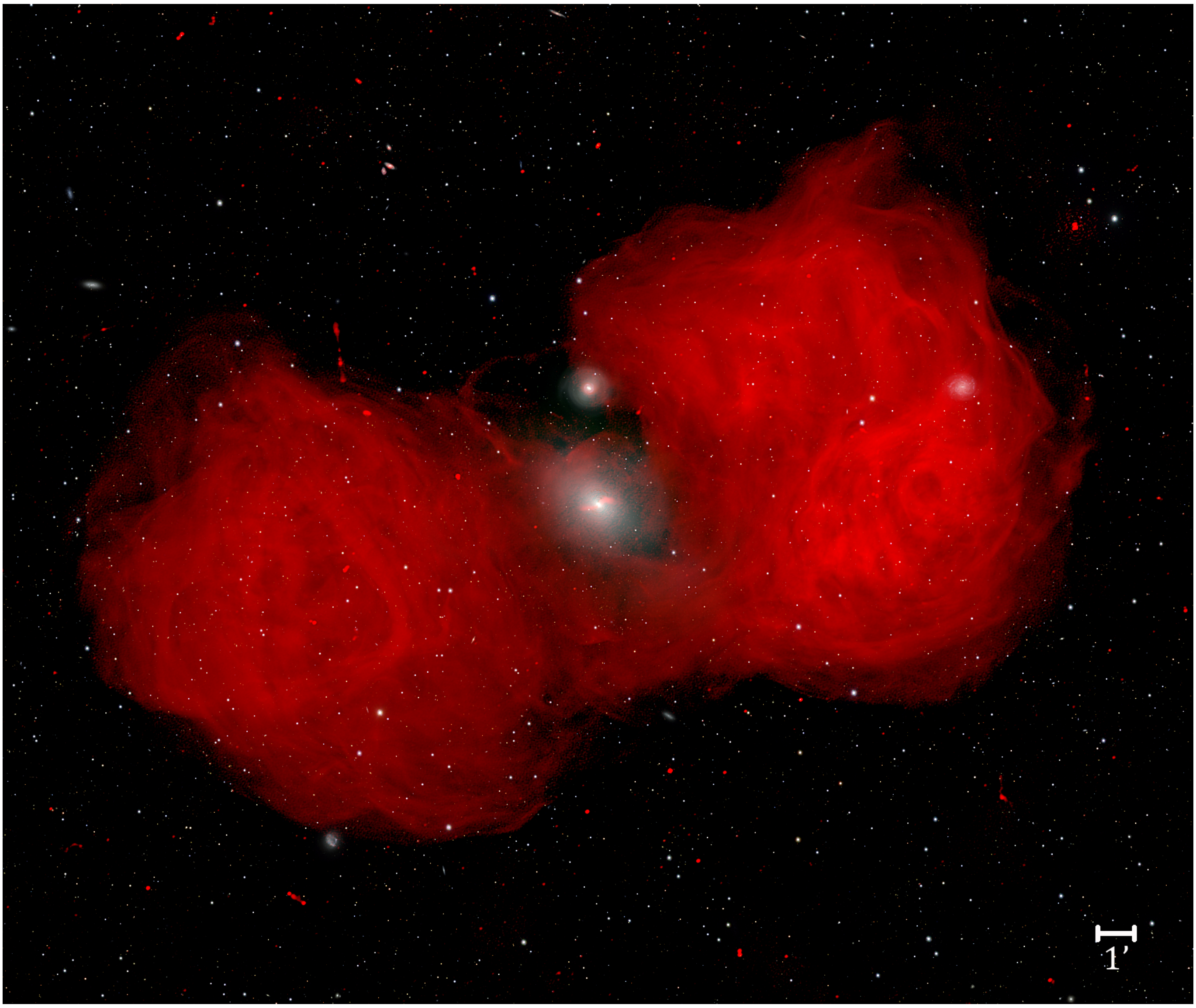


**Fig. 1.** Fornax A seen by MeerKAT at 1.44 GHz. The radio emission is in red, as well as the background and foreground sources. The three-colour composite image (from the *gri* bands) of the same field of view is taken from the Fornax Deep Survey (Iodice et al. 2017).

2 min. Shorter time intervals were found to produce noisier gain solutions with no improvement in the images, while longer time intervals failed to capture the gain variations in the data and caused low-level artefacts.

Given the large extent of the lobes of Fornax A (1.1°), in order to accurately study the properties of their radio spectrum it is crucial to correct the images with an accurate primary beam model. We created the primary beam Jones matrix of MeerKAT for any frequency of *L*-band observations, using `eidos` (Asad et al. 2019)[4]. From the Jones matrix we produced the images of the real and imaginary parts of the primary beam self-correlations (*xx* and *yy*). Their combination results in the image of the primary beam in the same field of view and with the same pixel size as the continuum images. We obtained the primary beam-corrected images by dividing the continuum images by the primary beam images at the corresponding frequency.

Figure 1 shows the radio emission of Fornax A seen by MeerKAT at 1.44 GHz overlaid on the deep photometric image from the Fornax Deep Survey (FDS) three-colour composite (from the *gri* bands; Iodice et al. 2017). The average noise in the 2° field of view is 16 $\mu$ Jy beam$^{-1}$. The dynamic range of the image (defined as the ratio between the peak emission of Fornax A and the noise in the image) is approximately 7000. This, along with the complete *uv*-coverage of MeerKAT over short ($\lesssim$50 m), as well as long ($\gtrsim$2 km) baselines allows us, for the very first time, to detect with high resolution (6.8″ × 5.8″, PA= 117°) and signal-to-noise ratio ($S/N > 20$) the diffuse emission at the edges of the radio lobes. In the same short (~8 h) observation, we also spatially resolve the central emission and the filaments of the lobes. Figure 2 shows the radio emission of Fornax A at 1.03 GHz. The image has similar resolution (11.2″ × 9.1″, PA= 119°) and sensitivity (noise ~28 $\mu$ Jy beam$^{-1}$) as the image at 1.44 GHz. Only in the proximity of bright ($\gtrsim$15 m Jy beam$^{-1}$) sources at about 1 degree from the phase centre (where the response of the MeerKAT antennas drops), the noise increases because of direction-dependent calibration effects. We did not attempt to correct for such effects.

The images obtained from the MeerKAT observation allow us to reveal the double-shell structure of the lobes of Fornax A,

[4] https://github.com/ratt-ru/eidos

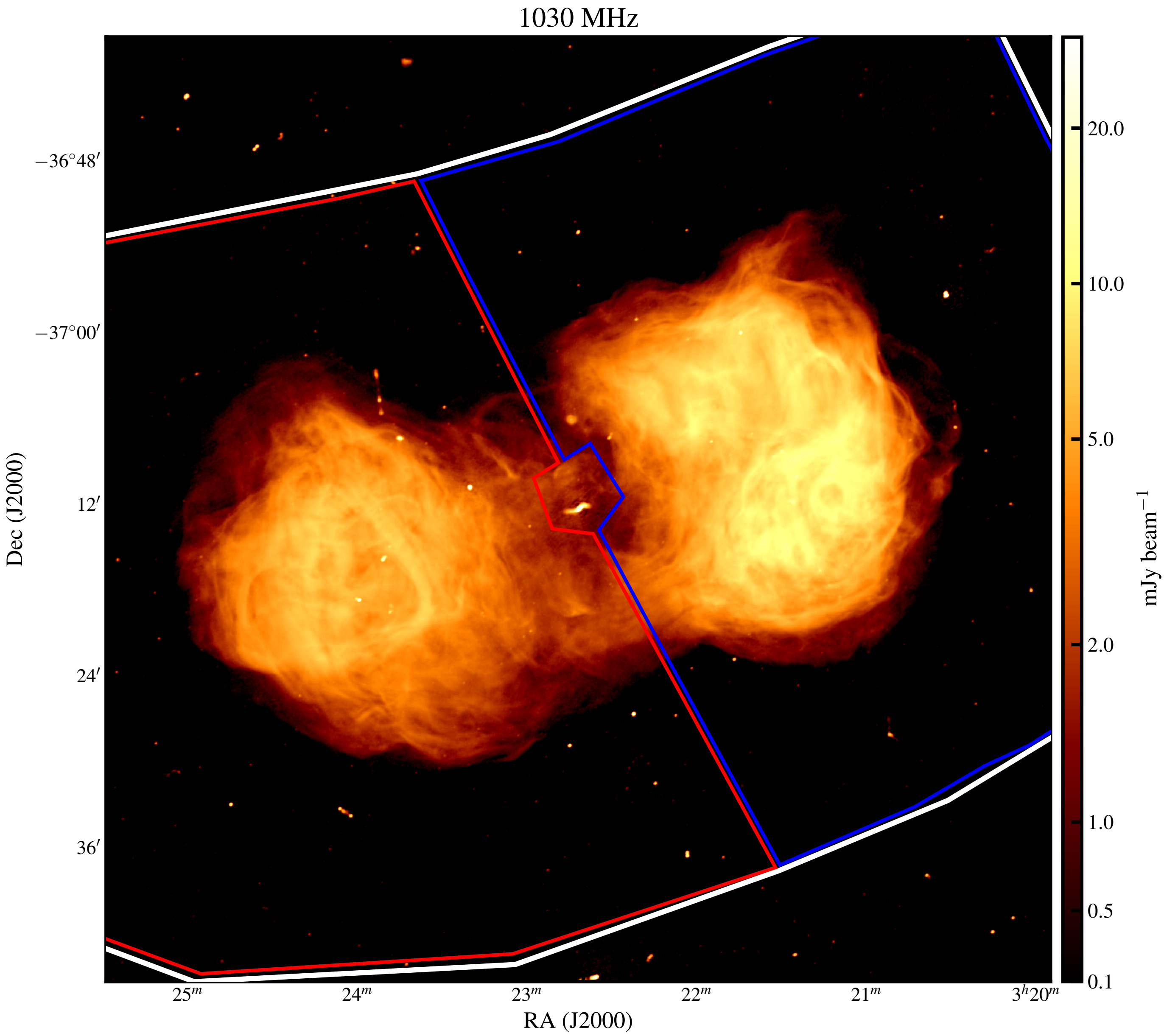


**Fig. 2.** Fornax A seen by MeerKAT at 1.03 GHz. The white contours mark the region where we measure the total flux density of the source, and the red and blue contours mark the regions of the east and west lobes, respectively. The synthesized beam of the image is $11.2'' \times 9.1''$.

where the bright filaments appear embedded in a diffuse cocoon. For the first time, we are able to study the spectral properties of this double-shell structure and understand how the lobes of Fornax A may have formed.

### 2.2. SRT: 5.7 GHz–6.9 GHz

Fornax A was observed with the SRT on January 26 and February 7, 2017. These observations were conducted in the context of the development of the spectral-polarimetric wide-field imaging of the SARDARA backend (SArdinia Roach2-based Digital Architecture for Radio Astronomy; Melis et al. 2018). The total observing time on target was 4.5 h. We performed several on-the-fly (OTF) mappings in the equatorial frame in both right ascension and declination. We imaged a field of view of $1.2^\circ \times 1.2^\circ$ using four RA and three Dec scans. The average angular resolution of the SRT at this frequency is $FWHM = 3.0'$ so we set the telescope scanning speed to $6'\ \mathrm{s}^{-1}$ and the scan separation to $42''$ to properly sample the beam. The correlator configuration was set to 1024 frequency channels (2.2 MHz-wide) for a total bandwidth of 2300 MHz in full-Stokes mode. We set the Local Oscillator to 5600 MHz and used a filter to select the frequency range 5700–6945 MHz, which is relatively free from strong radio frequency interference.

Data reduction was performed with the proprietary Single-dish Spectral-polarimetry Software (`SCUBE`; Murgia et al. 2016). Bandpass and flux density calibration were performed by observing respectively 3C 138 and 3C 295, assuming the flux density scale of Perley & Butler (2013a). Persistent radio frequency interference (RFI) was flagged and we applied the gain-elevation curve correction to account for the gain variation with elevation due to the change in telescope structure as a result of gravitational stress. In band $C$, SRT observations are only moderately affected by atmospheric absorption which depends on the

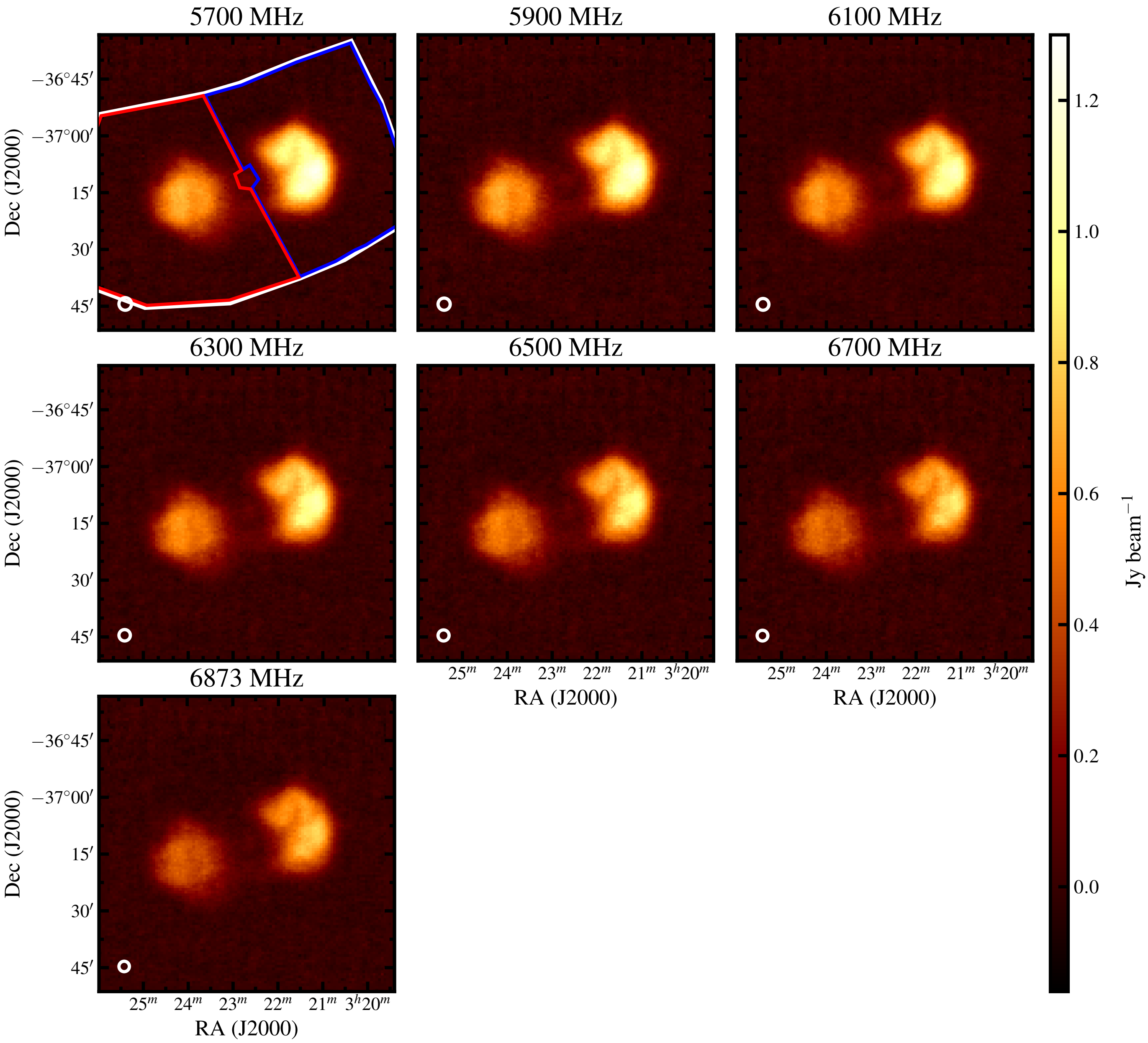


**Fig. 3.** Fornax A seen between 5.7 and 6.87 GHz by the SRT. *Top left panel*: the contours mark the regions where we measure the total flux density and the flux density of the lobes (in white, red and blue, respectively). The synthesized beam of the images is shown in white in the bottom left corner of each panel.

weather conditions at the telescope site and on the elevation of the source. At the time of the observations, the opacity ($\tau$) was 0.008 and 0.009, respectively. Since, Fornax A had elevation ($el$) $\lesssim 15°$, the opacity correction to the flux density is:

$$k = \left(e^{\frac{-\tau}{\sin(el)}}\right)^{-1} = 1.05. \quad (1)$$

We performed the polarisation calibration by correcting the instrumental polarisation and the absolute polarisation angle.The on-axis instrumental polarisation was determined through observations of the bright unpolarised source 3C 84. The leakage of Stokes $I$ into $Q$ and $U$ is in general less than 2% across the band, with a rms scatter of 0.7–0.8%. We fixed the absolute position of the polarisation angle using as reference the primary polarisation calibrator 3C 138. The difference between the observed and predicted position angle according to Perley & Butler (2013b) was determined, and corrected channel-by-channel.

All frequency cubes obtained by gridding the scans along the two orthogonal axes (RA and Dec) were then stacked together to produce full-Stokes $I$, $Q$, $U$ images of an area of 1.2 square degree centred on Fornax A. In the combination, the individual image cubes were averaged and de-stripped by mixing their stationary wavelet transform (SWT) coefficients (see Murgia et al. 2016, for details). For the purposes of this work we further averaged the total intensity spectral cube into seven sub-bands of about 200 MHz in width. The resulting images are shown in Fig. 3, their noise varies between 7.2 and 6.0 mJy beam$^{-1}$ (see Table 2). We used these observations only to analyse the emission of the radio lobes of Fornax A, since the SRT beam does not resolve the central radio emission of Fornax A.

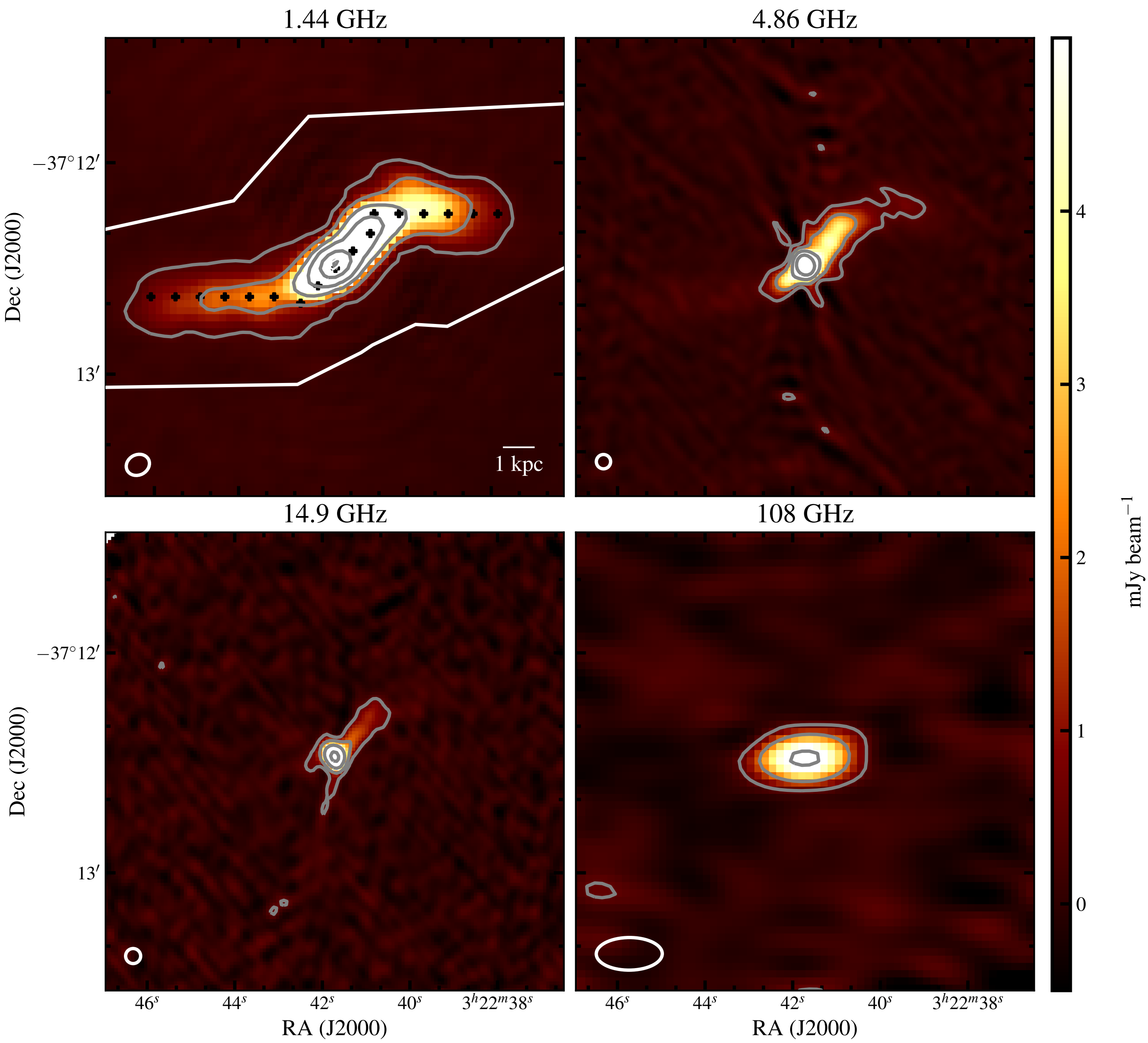


**Fig. 4.** Central emission of Fornax A seen at 1.44 GHz by MeerKAT (*top left panel*), at 4.86 GHz (*top right panel*), 14.9 GHz (*bottom left panel*) by the VLA and at 108 GHz (*bottom right panel*) by ALMA. The PSF of the images is shown in white in the bottom left corner. Contour levels start at 0.6 mJy beam$^{-1}$, increasing by factors of three. In the *top left panel*, the black dots show where we measured the variations in flux density and width along the jets (see Sect. 4 for further details).

### 2.3. ALMA: 108 GHz

Observations of Fornax A centred at 108 GHz were carried out during cycle 5 as part of an ALMA survey of 65 galaxies in the Fornax cluster (PI Kana Morokuma-Matsui, project code 2017.1.00129.S) These observations were taken during an observing campaign that lasted from October 16 to December 21, 2017, and consist of ten different pointings of the ALMA-Morita array within the innermost 2′ × 3′ of Fornax A (∼12 × 18 kpc). The chosen array configuration has baselines ranging from 8.9 m to 48.9 m. The main goal of these observations was to observe the distribution and kinematics of the molecular gas in NGC 1316, as traced by the CO(1–0) line at $\nu_{\rm rest}$ = 115.27 GHz (Morokuma-Matsui et al. 2019). Three spectral windows, each of 2 GHz in width, were dedicated to continuum studies (centred at 113.39 GHz , 103.27 GHz, and 101.39 GHz, respectively). The continuum image shown in Fig. 4 (bottom right panel) was generated considering all four spectral windows of the observation, where the frequency range of the detected $^{12}$CO (1–0) line emission and of the tentative detection of the CN hyper-fine transitions at 112.85 GHz have been flagged. This image allows us to estimate the flux density of the continuum emission in the innermost kiloparsec of Fornax A in the millimetre band.

The calibration of the Morita-Array observations was conducted with the ALMA pipeline version 40896 (Pipeline CASA51-P2-B; Petry & CASA Development Team 2017) at the Joint ALMA Observatory (JAO). The continuum image was generated using `CASA`. In particular, we used the task `tclean` with `Briggs` weighting and `robust` parameter 0.5.

We performed cleaning using the `hogbom` algorithm within a mask selected by standard `auto-threshold` and mosaicking options (`sidelobethreshold` = 1.25, `noisethreshold` = 5, `meanbeamfrac` = 0.1, `lownoisethreshold` = 2.0, `negative-threshold` = 0.0, `gridder` = "mosaic"). The synthesized beam is 18.1″ × 9.0″ (∼1.8 × 0.99 kpc) with PA = −89°, and the noise is 0.21 mJy beam$^{-1}$.

## 3. Radio flux density of Fornax A

In this section we measure the flux density distribution of the radio lobes of Fornax A between 84 MHz and 217 GHz, and of the central emission between 1.03 and 108 GHz.

### 3.1. The lobes

We analyse the properties of the radio lobes of Fornax A separately. The regions enclosing the east and west lobes are shown in Fig. 2. We define the regions large enough to cover the radio lobes at all frequencies. The figure also shows the region where we measure the total flux of Fornax A (that is dominated by the emission of the two lobes). We use this measurement to compare our results to those in the literature (McKinley et al. 2015; Perley & Butler 2017), where the analysis of the flux density distribution was performed on the sum of the emission of the two lobes (see Appendix A for further details).

Before measuring the flux, all images are corrected for the primary beam response and re-projected to the same reference frame. In each image, the noise per beam is equal to the dispersion of the signal in the field of view, once all sources have been excluded. This is a reliable measurement of the noise only if it has constant power spectrum density (i.e. white noise). This is the case for all considered observations except for the images taken from the full-sky *Planck* foreground maps. The background of the *Planck* images is not flat, but has large nonzero patches. We include those large-scale fluctuations of the background in our estimate of the Fornax A flux uncertainties. The origin of those patches could be related to the background-subtraction process. To obtain a reliable estimate of the error on the *Planck* flux densities of Fornax A, we extracted the images on a large field of view (∼4 degrees), and measured the error on the flux density as the dispersion of the flux density of 100 independent regions in the field of view of shape and size equal to the regions where we measured the flux density of the lobes (Fig. 2). Further details on the reduction and analysis of the *Planck* observations are given in Appendix A.3.

The total flux density of Fornax A and the flux densities of the east and west lobes with errors are shown in Table 3. At each frequency, the error on the flux density is the combination between the noise in the image (shown in Table 2 for each observation) and the error due to the uncertainties in the calibration of the observations, which is 20% for MWA (McKinley et al. 2015), 15% for *Planck* (Planck Collaboration IV 2020), 5% for SRT (Egron et al. 2017; Battistelli et al. 2019) and 3% for VLA (Perley & Butler 2017), respectively. For the MeerKAT observation we estimate a flux-calibration error of 5% to allow for uncertainties in the flux of the gain calibrator. Archival observations from the VLA and MWA are on the Baars et al. (1977) flux density scale, *Planck* observations are on an absolute flux density scale (Partridge et al. 2016), while MeerKAT, SRT, and ALMA observations have been calibrated according to Perley & Butler (2017). Discrepancies caused by these different scales are typically on the order of ∼1–3%, and are within the errors we assume on the flux density measurements.

**Table 3.** Total flux density of Fornax A, and of the east and west lobes.

| Frequency [GHz] | East lobe [Jy] | West lobe [Jy] | Total [Jy] |
|---|---|---|---|
| 0.84 | 276 ± 55 | 504 ± 101 | 788 ± 158 |
| 0.118 | 237 ± 48 | 448 ± 89 | 692 ± 138 |
| 0.154 | 229 ± 46 | 387 ± 77 | 624 ± 125 |
| 0.200 | 185 ± 37 | 341 ± 68 | 533 ± 107 |
| 0.320 | 106 ± 5 | 236 ± 12 | 345 ± 17 |
| 1.03 | 61 ± 3 | 101 ± 5 | 163 ± 8 |
| 1.44 | 47 ± 2 | 80 ± 4 | 128 ± 6 |
| 1.50 | 41 ± 2 | 78 ± 4 | 121 ± 6 |
| 5.80 | 16 ± 1 | 26 ± 1 | 44 ± 2 |
| 5.90 | 16 ± 1 | 27 ± 1 | 44 ± 2 |
| 6.10 | 16 ± 1 | 27 ± 1 | 44 ± 2 |
| 6.30 | 16 ± 1 | 27 ± 1 | 44 ± 2 |
| 6.50 | 16 ± 1 | 26 ± 1 | 43 ± 2 |
| 6.70 | 15 ± 1 | 25 ± 1 | 41 ± 2 |
| 6.87 | 15 ± 1 | 24 ± 1 | 39 ± 2 |
| 30 | 3.7 ± 0.6 | 4.6 ± 0.7 | 8.5 ± 1.3 |
| 44 | 2.0 ± 0.3 | 2.5 ± 0.4 | 4.6 ± 0.7 |
| 70 | 1.2 ± 0.3 | 1.7 ± 0.4 | 2.9 ± 0.5 |
| 100 | 0.4 ± 0.3 | 0.6 ± 0.2 | 0.9 ± 0.4 |
| 143 | (0.4) | 0.3 ± 0.3 | 0.3 ± 0.5 |
| 217 | (0.3) | (0.6) | (0.7) |

**Notes.** 1$\sigma$ upper limits are shown within parenthesis, at the frequencies where the lobes are not detected.

Figure 5 shows the flux density of the radio lobes and the total radio emission of Fornax A. As shown in Fig. B.1 and in Table B.1, over the frequency range in common, the measurements of this work are consistent with the measurements of McKinley et al. (2015) and Perley & Butler (2017). Further details are given in Appendix B.

### 3.2. The central emission

The central radio emission of Fornax A is clearly visible in the MeerKAT images (see Figs. 1, 2 and 4). At 4.8 GHz and 14 GHz, this emission is still visible in VLA images (see the top right and bottom left panel of Fig. 4). The ALMA image does not show significant extended emission beyond the central synthesized beam (18.1″ × 9.0″, see the bottom right panel of Fig. 4). Given the morphology of the central emission, we measure its flux density by dividing it into two parts, the central unresolved component (hereafter, the *kpc-core*) and the extended component forming the emission (the *jets*).

To measure these flux densities, we regrid all images to a common frame of reference and we convolve them to the lowest resolution of the sample (18.1″ × 18.1″). We define a region including the emission in all images (see the top left panel of Fig. 4). Since the kpc-core is unresolved, its flux density is equal to the peak flux within the central synthesized beam. The flux density of the jets is the sum of the emission in the selected region minus the flux density of the kpc-core. Table 4 shows the flux densities of both components at all selected frequencies. The spectrum of the two components is shown in the right panel of Fig. 5. The spectral shape of the extended component is much steeper than that of the kpc-core.

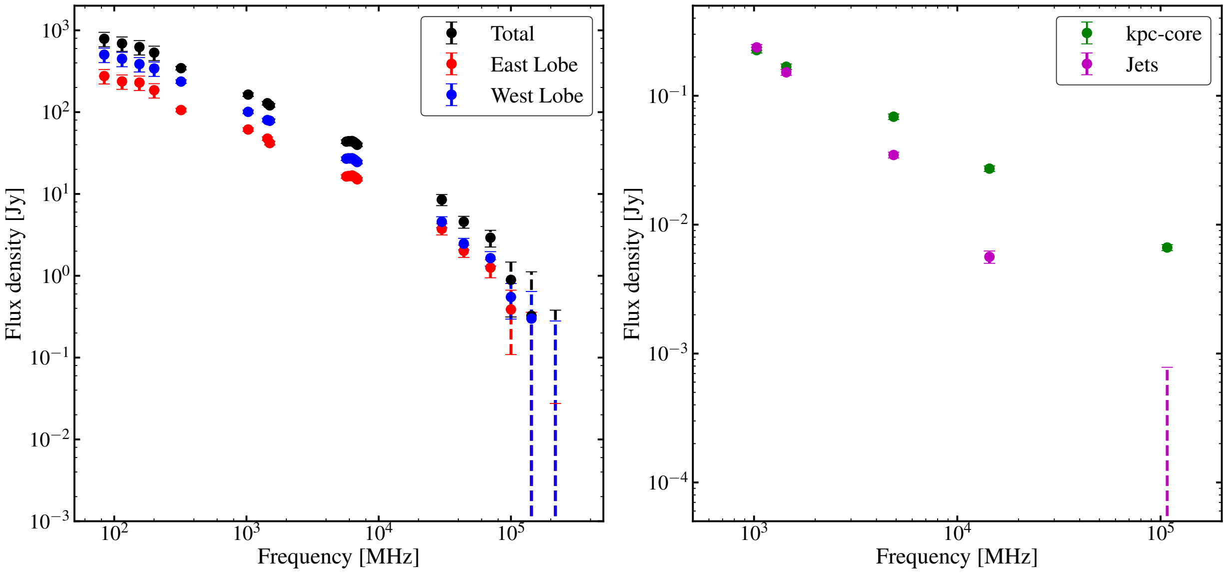


**Fig. 5.** *Left panel*: total flux density distribution of Fornax A between 84 MHz and 217 GHz (in black) and of the east and west lobes (in red and blue, respectively). The dashed error bars represent $1\sigma$ upper limits at the frequencies where the lobes are not detected. *Right panel*: flux density distribution of the kpc-core (green) and of the jets (magenta) of the central emission of Fornax A between 1.03 and 108 GHz.

**Table 4.** Flux density of the central emission of Fornax A.

| Frequency [GHz] | kpc-core [mJy] | Jets [mJy] |
|---|---|---|
| 1.03 | 156 ± 8 | 238 ± 12 |
| 1.44 | 105 ± 5 | 152 ± 8 |
| 4.86 | 43 ± 2 | 35 ± 2 |
| 14.4 | 20 ± 1 | 6 ± 1 |
| 108 | 6.7 ± 0.4 | (0.0007) |

**Notes.** We refer to the unresolved component as the kpc-core and to the extended component as jets. $1\sigma$ upper limit is shown within parenthesis at 108 GHz, where the jets are not detected.

## 4. Properties of the jets of Fornax A

We analyse the morphology and brightness distribution of the central emission of Fornax A that we can infer from the high-resolution observation at 1.44 GHz (see the top left panel of Fig. 4). In the previous section, we separated the central emission into two components, the unresolved kpc-core and the extended jets. Another way to decompose the central emission consists of considering the *jet* as the emission in the northwest of the core and the *counter-jet* as the emission in the southeast. Both jet and counter-jet expand symmetrically away from the nucleus with a position angle of 135° (north through east). At the distance of ~2.5 kpc, both jets bend in the east–west direction, then fade below the $5\sigma$ detection limit (~80 $\mu$ Jy beam$^{-1}$) at distances above 6 kpc from the nucleus.

To characterise the jets we measure their variations of transverse size and surface brightness with increasing distance from the AGN. We fitted a single Gaussian to the one-dimensional profiles extracted at intervals of 8″ (approximately half the beam of the image) in the direction perpendicular to the jet expansion. This gives us the measured profile width ($w_0$) and peak ($I_0$) as a function of radius. We corrected these values for the effect of the beam width ($w_\mathrm{b}$), as in Laing et al. (1999):

$$w = \sqrt{w_0^2 - w_\mathrm{b}^2} \quad I = I_f \sqrt{w^2/w_\mathrm{b}^2 + 1}, \tag{2}$$

obtaining the corrected values of transverse size ($w$) and surface brightness $I$ as a function of radius.

In the top left panel of Fig. 6, we show the peak surface brightness of the jet and counter-jet against the radial distance from the core, which shows that the jet is typically brighter than the counter jet. The bottom left panel of the figure shows that in the innermost ~2.5 kpc the jet has between approximately two and six times the surface brightness of the counter-jet. This ratio reaches its maximum value in proximity to where the jets bend ($I_j/I_\mathrm{cj} \sim 6$), then it decreases with distance from the nucleus. Overall the brightness ratio is always lower than four suggesting that the jets are "two-sided" (Bridle & Perley 1984; Bridle et al. 1991).

The bottom right panel of the figure shows the transverse size of the jet and counter-jet with distance from the core in logarithmic scale. The ratio between the size of the jet and counter-jet is maximal where the jets bend, and then decreases with distance from the centre.

In the top right panel of Fig. 6, we show the brightness versus the transverse size of the jet and counter-jet, and the model (dashed black line) that these quantities should follow if the jets were undergoing adiabatic expansion at constant velocity and spectral index (a power law with spectral index $\beta \sim -3.4$; Laing et al. 1999; Parma et al. 1999). The main outliers from this curve are points tracing the innermost part of the jets ($r \lesssim 5$), before they bend in the east–west direction. After this bend, it is possible that the jets are freely expanding. The central emission may have been generated by precessing jets. S-symmetric bent jets are a typical signature for this mechanism (Monceau-Baroux et al. 2014; Donohoe & Smith 2016; Krause et al. 2019).

Knowing the spectral index of the jets (see Sect. 6.2), and making an assumption on their velocity ($\beta$), it is possible to estimate their orientation ($\theta$) with respect to the plane of the sky ($\theta = 0$). The ratio of the flux density of the jets depends on $\theta, \beta$ and their spectral index as (Bridle & Perley 1984; Parma et al. 1987):

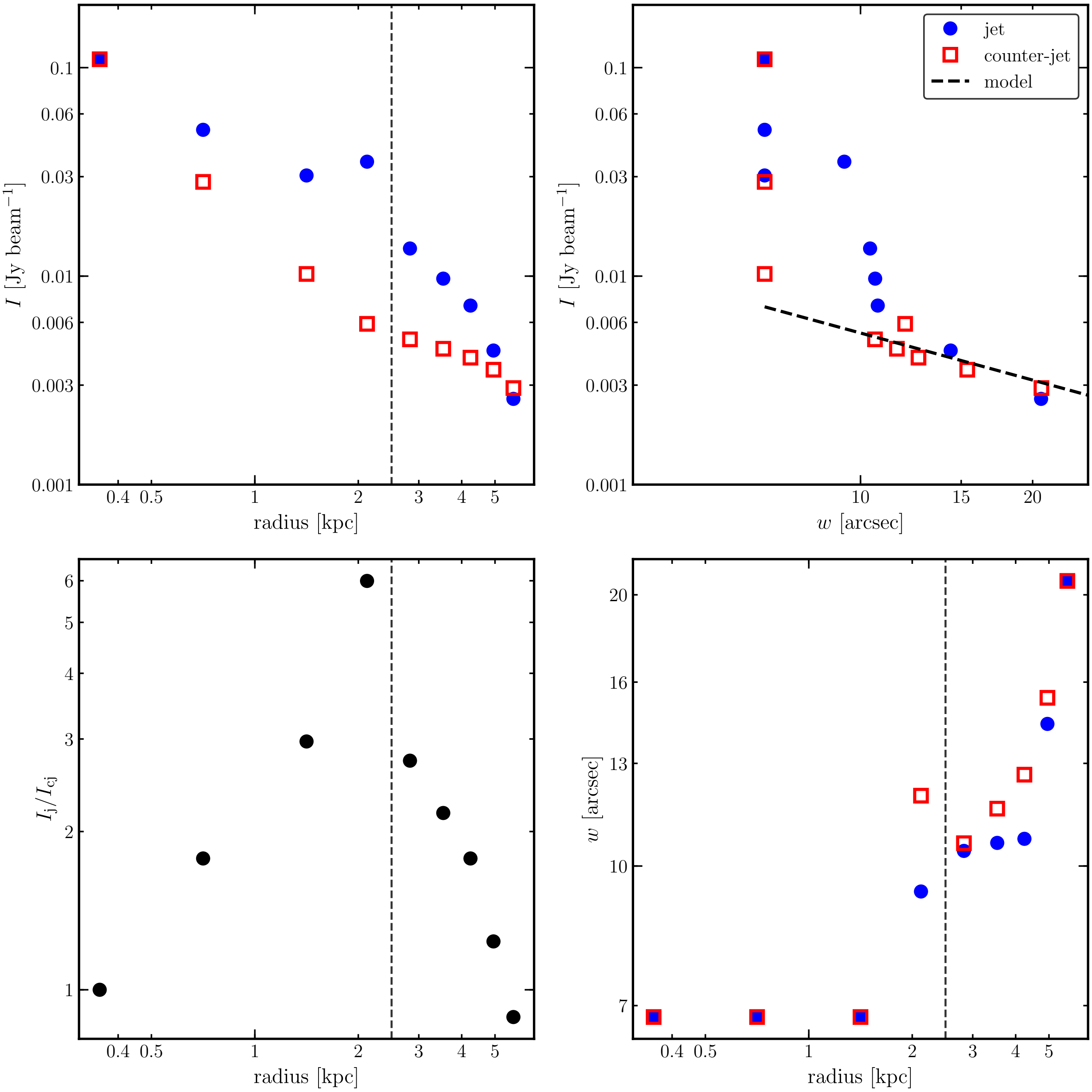


**Fig. 6.** *Top left panel*: surface brightness vs. radial distance from the core to the jet (blue circles) and counter-jet of Fornax A (red squares). The dashed vertical line marks the radius where the jets bend in the east–west direction. *Top right panel*: surface brightness of the jet and counter-jet vs. transverse size. The dashed line shows the predicted distribution if the jets were adiabatically expanding. *Bottom left panel*: surface brightness ratio between jet and counter-jet vs. radial distance from the core. *Bottom right panel*: transverse size of the jet and counter-jet vs. radial distance from the core. Colours are as in the top panels.

$$\frac{I_{\rm j}}{I_{\rm cj}} = \left(\frac{1+\beta\cos\theta_0}{1-\beta\cos\theta_0}\right)^{3+\alpha}. \quad (3)$$

Assuming $\alpha_{\rm inj}$ (jets) = 0.6 (as we infer from our model) the orientation angle is $\langle\theta\rangle \leq 30°$, for values of $\beta$ between 0.4 and 0.9$c$ (which are realistic velocities for jets expanding in the ISM; Parma et al. 1987; Bridle et al. 1991; Churazov et al. 2001). The orientation of the jets is likely approximately in the plane of the sky, and the jet in the northwest is coming towards the observer.

Assuming that the radio emission contains relativistic particles confined in a uniformly distributed magnetic field in energy equipartition conditions (Kardashev 1962; Bridle & Perley 1984), it is possible to estimate the magnetic field strength (in Gauss) as:

$$B_{\rm eq} = 9.6\times10^{-12}\left(\frac{P_{1.4\,{\rm GHz}}(1+k)}{V^3}\right)^{2/7}, \quad (4)$$

where the radio power at 1.4 GHz ($P_{1.4\,{\rm GHz}}$) is expressed in W Hz$^{-1}$, $k$ is the ratio between the energy of protons and electrons in the radio emitting region (assumed equal to 1), and $V$ is the volume of the emitting region in kpc$^3$.

We determine the equipartition magnetic field of the kpc-core and of the jets (see Table 5). We assume that an upper limit

**Table 5.** Mean properties of the jets and the kpc-core of Fornax A inferred from the MeerKAT observation.

| Parameter | Value |
|---|---|
| $P_{1.4\,\mathrm{GHz}}$ (kpc-core) | $5.5\times10^{22}$ W Hz$^{-1}$ |
| $P_{1.4\,\mathrm{GHz}}$ (jets) | $1.1\times10^{23}$ W Hz$^{-1}$ |
| $\langle FWHM\rangle$ (jet) | 14″ |
| $\langle FWHM\rangle$ (counter−jet) | 20″ |
| $\langle B_{\rm eq}\rangle$ (kpc-core) | $\gtrsim 50\,\mu$G |
| $\langle B_{\rm eq}\rangle$ (jets) | $\gtrsim 23\,\mu$G |
| $\langle u_{\rm min}\rangle$ (kpc-core) | $\gtrsim 2.3\times10^{-10}$ erg cm$^{-3}$ |
| $\langle u_{\rm min}\rangle$ (jets) | $\gtrsim 4.9\times10^{-11}$ erg cm$^{-3}$ |
| $\langle\Theta\rangle$ (opening angle) | $\lesssim 30°$ |

to the volume of the kpc-core region is given by the volume of an ellipsoid with axes equal to the beam of the image at 108 GHz, which is the lowest resolution with which we image the kpc-core ($x$ = 18″, $y$ = 9″, $z$ = 18″). The magnetic field of equipartition of the kpc-core is $B_{\rm eq,\,kpc-core}\gtrsim 50\,\mu$G. The jets extend in the plane of the sky for approximately 6 kpc in each direction (see the upper left panel of Fig. 6). We assume that the jets occupy a cylindrical volume of length 12 kpc and width given by the average size of the jet and counter-jet (20″, 2.02 kpc). This gives us an upper limit to the magnetic field of $B_{\rm eq,\,jet}\gtrsim 23\,\mu$G.

The total energy of a synchrotron source is given by the energy of the relativistic particles plus the energy of the magnetic field in which they are embedded. The energy is minimum when the contributions of magnetic fields and relativistic particles are approximately equal, that is the equipartition condition (Pacholczyk 1970). Therefore, from the equipartition magnetic field we can estimate the minimum energy of the jets: $B_{\rm eq}=\sqrt{24\pi/7\,u_{\rm min}}$. We estimate $u_{\rm min,\,kpc-core}\gtrsim 2.3\times10^{-10}$ erg cm$^{-3}$ and $u_{\rm min,\,jets}=4.9\times10^{-11}$ erg cm$^{-3}$. If the jets were confined by the external medium, these minimum energies would require the ISM to have $n_{\rm e}T_{\rm e}\sim4\times10^{4}$ K cm$^{-3}$. In the innermost 200″ (21.7 kpc) of Fornax A, X-ray observations have observed the presence of two cavities broadly aligned with the jets (Isobe et al. 2006; Lanz et al. 2010). The *Chandra* spectrum of the X-ray emission in the innermost 15 kpc provides an estimate of the temperature and density of the ISM of 0.77 keV ($8.9\times10^{6}$ K) and 0.4 cm$^{-3}$ (Nagino & Matsushita 2009), exceeding the minimum $n_{\rm e}\,T_{\rm e}$ value required for jet confinement by two orders of magnitude. Therefore, the pressure in the central region of Fornax A is sufficient to confine the jets. The properties of the jets that we derived in this section are summarised in Table 5.

## 5. Spectral analysis of the main components of Fornax A

To estimate the timescale of formation of the radio lobes of Fornax A and disentangle the different phases of the nuclear activity, we study the spectrum of the integrated radio emission of the lobes and of the centre. Assuming that radiative energy losses from synchrotron (s) and inverse Compton (ic) radiation dominate over expansion losses, and by excluding in situ injection or re-acceleration of the relativistic electrons in the lobes (besides those provided by the central engine through the radio jets), the radio spectrum shows a sharp cut-off whose frequency depends on the age of the radiation and its history of injection (e.g. Kardashev 1962; Pacholczyk 1970; Slee et al. 2001; Murgia et al. 1999, 2011; Harwood et al. 2013). A general equation describing the variation of the energy distribution of particles in a confined volume is given by the continuity equation:

$$\frac{\partial N(\epsilon,t)}{\partial t}+\frac{\partial}{\partial\epsilon}\left(\frac{\partial\epsilon}{{\rm d}t}N(\epsilon,t)\right)+\frac{N(\epsilon,t)}{T_{\rm conf}}=Q(\epsilon,t),\tag{5}$$

where $N(\epsilon,t)$ is the number of particles of energy $\epsilon$ at the time $t$. $N(\epsilon,t)/T_{\rm conf}$ indicates the frequency with which particles can escape the volume and $Q(\epsilon,t)$ represents the continuous injection of particles into the volume till the time $t$. Here, we assume that the relativistic particles injected by the AGN do not escape the radio lobes or jets, $T_{\rm conf}=\infty$. Following Kardashev (1962), the lobes (or jets) are continuously injected with particles (continuous injection model, CI) with energies distributed in a power law:

$$Q(\epsilon,t)=A\epsilon^{-\delta},\tag{6}$$

while the radiative losses can be expressed as:

$$\left(\frac{{\rm d}\epsilon}{{\rm d}t}\right)_{\rm s,ic}=b(B^2+B^2_{\rm CMB})\epsilon^2=b_{\rm s,ic}\epsilon^2\propto B^2\epsilon^2,\tag{7}$$

where $b$ is a generic constant (Pacholczyk 1970). If we assume that inverse Compton losses are due to the cosmic microwave background and act as a magnetic field, $B^2_{\rm CMB}=8\pi u_{\rm CMB}$ (where $u_{\rm CMB}$ is the energy density of the radiation), then $b(B^2+B^2_{\rm CMB})=b_{\rm s,ic}$. We assume that the distribution of electrons stays isotropic during its losses, which is known as the Jaffe & Perola approximation (JP; Jaffe & Perola 1973). Under this approximation the timescale for continuous isotropisation of the electrons is much shorter than their radiative lifetime, and their losses do not depend on the actual pitch angle but rather on an average performed over all possible angles that they have travelled since the injection. The losses depend on the magnetic field in the direction perpendicular to the motion of the electrons:

$$b_{\rm s,ic}=2.37\times10^{-3}\cdot(2/3)\cdot B^2_{\perp}.\tag{8}$$

Under these assumptions, the number of particles of energy $\epsilon$ at a given time $t$ is given by the solution of Eq. (5):

$$\begin{aligned}N(\epsilon,t)&\approx A\cdot\epsilon^{-\delta}\cdot t, && \epsilon<\epsilon^\star=\frac{1}{b_{\rm s,ic}t}\\ &\approx\frac{A}{\delta-1}\cdot\frac{\epsilon^{-(\delta+1)}}{b_{\rm s,ic}}, && \epsilon\gtrsim\epsilon^\star=\frac{1}{b_{\rm s,ic}t}.\end{aligned}\tag{9}$$

In the spectrum of the CI model, $J_{\rm s}(\nu)$, two power-law regimes can be identified:

$$\begin{aligned}J_{\rm s}(\nu)&\propto\nu^{-(\delta-1)/2}=\nu^{-\alpha_{\rm inj}}, && \nu<\nu_{\rm break}\\ &\propto\nu^{-\delta/2}=\nu^{-(\alpha_{\rm inj}+1/2)}, && \nu\gtrsim\nu_{\rm break}.\end{aligned}\tag{10}$$

At low energies (below the break-frequency, $\nu_{\rm break}$), the spectral index is $\alpha_{\rm inj}=\frac{\delta-1}{2}$, while at high energies ($\nu\gtrsim\nu_{\rm break}$) the index is $\alpha_{\rm high}=\alpha_{\rm inj}+1/2$. The cutoff frequency depends on the time since the injection began, that is the radiative age of the source $t_{\rm s}$ (e.g. Murgia et al. 2010b; Orrù et al. 2010; Harwood et al. 2013):

$$t_{\rm s}=1610\frac{B^{0.5}}{B^2+B^2_{\rm CMB}}\frac{1}{[\nu_{\rm break}(1+z)]^{1/2}}.\tag{11}$$

A more complicated scenario describing the radiation of the lobes and jets of Fornax A can be the continuous injection plus turn off model (CI$_{\rm OFF}$). The injection of high-energy particles from the nucleus starts at $t = 0$ and at the time $t_{\rm CI}$ it is switched off ($Q(\epsilon, t_{\rm CI}) = 0$). After that, a new phase of duration $t_{\rm OFF}$ begins (i.e. the *off phase* of the AGN), and $t_{\rm s} = t_{\rm CI} + t_{\rm OFF}$ (e.g. Slee et al. 2001; Parma et al. 2007; Murgia et al. 2011). Compared to the CI model, the spectral shape is characterised by a second break-frequency ($\nu_{\rm break,\,high}$), beyond which the radiation spectrum drops exponentially. This frequency depends on the ratio between the dying phase and the total age of the source ($t_{\rm s}/t_{\rm OFF}$):

$$\nu_{\rm break,\,high} = \nu_{\rm break}\left(1 + \frac{t_{\rm CI}}{t_{\rm OFF}}\right)^2 = \nu_{\rm break}\left(\frac{t_s}{t_{\rm OFF}}\right)^2. \quad (12)$$

The longer the source has been off, the shorter the distance between the two break-frequencies.

In the following sections, we determine whether the radio lobes and the kpc-core and jets of Fornax A are best described by a continuous injection model (CI) or by a continuous injection plus turn-off model ($\rm CI_{OFF}$). We measure the break-frequency ($\nu_{\rm break}$) injection index ($\alpha_{\rm inj}$), and eventually $t_{\rm OFF}/t_{\rm start}$, which define the spectral shape of the different components and we estimate the age of their synchrotron radiation. Furthermore, we study the variations of the spectral shape through the lobes and jets and present a map of the break-frequency used to constrain their injection history.

To determine the best-fit models, we use the software package `SYNAGE++` (Murgia et al. 1999), that has been used to measure the age of the relativistic electrons for several radio AGNs (e.g. Parma et al. 1999; Murgia 2003; Murgia et al. 2010b, 2011, 2012; Orrù et al. 2010; Kolokythas et al. 2015).

### 5.1. Spectral modelling of the lobes

Figure 7 shows the CI and $\rm CI_{OFF}$ models that best fit the radio spectrum of the east and west lobes. At ≳143 GHz both lobes are undetected, marking a sharp cut-off in the spectrum. The best-fit parameters for both models are listed in Table 6. We use the reduced-chi-squared to determine which model best fits the spectrum. For both lobes, the reduced-chi-squared ($\tilde{\chi}^2$) of the $\rm CI_{OFF}$ model has values closer to 1 than the $\tilde{\chi}^2$ of the CI model. This, along with the sharp cut-off at high frequencies, suggests that the radio spectrum of both radio lobes is best described by the $\rm CI_{OFF}$ model and that currently the radio lobes are not being injected with relativistic particles.

According to the $\rm CI_{OFF}$ model, the injection spectral index of the particles in the east lobe is $\alpha_{\rm inj} = 0.57^{+0.02}_{-0.10}$, the break-frequency is $\nu_{\rm break,\,E} = 32^{+8}_{-27}$ GHz, and the dying-to-total-age ratio is $t_{\rm OFF}/t_{\rm s} = 0.49^{+0.08}_{-0.42}$. Assuming that the magnetic field of the lobes is $2.6 \pm 0.3\,\mu$G (Isobe et al. 2006; Tashiro et al. 2009) the radiative age of the lobe is $t_{\rm s,\,E} = 25^{+23}_{-19}$ Myr. Likely, in the last $t_{\rm OFF,\,E} = 12^{+2}_{-9}$ Myr (∼49% of the total lifetime of the AGN) the east lobe has not been replenished with relativistic particles.

The results obtained for the west lobe are compatible with the ones of the east lobe, $\alpha_{\rm inj} = 0.63^{+0.02}_{-0.04}$, $\nu_{\rm break,\,W} = 33^{+9}_{-26}$ GHz and $t_{\rm OFF}/t_{\rm s} = 0.53^{+0.18}_{-0.41}$. This gives $t_{\rm s,\,W} = 23^{+20}_{-17}$ Myr and $t_{\rm OFF,\,W} = 12^{+4}_{-8}$ Myr.

The best-fit $\rm CI_{OFF}$ models of the total spectrum and of the west lobe have $\tilde{\chi}^2 \lesssim 1$. This likely occurs because the model is not only always compatible with the measured fluxes within the errors, but it also falls very close to the measured fluxes all through the spectrum. The errors on the flux density at two frequencies observed with the same telescopes are not independent, which could bias the $\tilde{\chi}^2$ statistics. Nevertheless, for the purposes of this study the $\tilde{\chi}^2$ is a good indicator to determine which one between the CI or the $\rm CI_{OFF}$ model better fits the observed radio spectra.

The spectral index of the lobes of Fornax A measured between 115 MHz and 1140 MHz ($\alpha = 0.77 \pm 0.05$; McKinley et al. 2015) and from the X-ray Inverse Compton emission ($\alpha = 0.68$; Isobe et al. 2006; Tashiro et al. 2009) is overall slightly steeper than the injection index we measure. This occurs because the spectral index of the flux density of the lobes is the exponent for which a single power law effectively approximates the flux density distribution in a limited interval of frequencies below $\nu_{\rm break}$. On the contrary, the injection index describes a double power law with a high-frequency cut-off.

A fundamental assumption in estimating the radiative age of the radio source is that the magnetic field within the lobes is constant. In the lobes of Fornax A we assumed $B = 2.6 \pm 0.3\,\mu$G, as was measured from the simultaneous modelling of synchrotron emission and inverse Compton-scattered X-ray emission (Isobe et al. 2006; Tashiro et al. 2009). This value agrees with the magnetic field of equipartition ($B_{\rm eq} \sim 3.0\,\mu$G), derived assuming a volume of the lobes of ∼150 kpc$^3$, suggesting that the radio lobes are in a state of minimum energy. The value of the inverse Compton magnetic field estimated from the distance of the source is $B_{\rm IC} = 3.25(1 + z)^2 = 3.2\,\mu$G, implying a ratio of $B/B_{\rm IC} = 0.8$. Given these conditions, any deviation from the minimum energy assumption has only a moderate impact on the age estimate (Parma et al. 1999).

### 5.2. Spectral modelling of the central emission

In the left panel of Fig. 8, we show the results of the best-fit for both the CI and $\rm CI_{OFF}$ model for the flux density of the kpc-core. The right panel shows the results for the jets. The best-fit parameters for both the CI and the $\rm CI_{OFF}$ model are listed in Table 6. The reduced chi-squared of the fits suggests that the spectral distribution of the kpc-core is better described by the CI model rather than by the $\rm CI_{OFF}$. The jets are instead better fitted by the $\rm CI_{OFF}$. It is possible that the kpc-core is still being injected with high-energy particles, while this is not currently happening in the jets. This result holds as long as the thermal contamination of the 108 GHz flux of the kpc-core, poorly constrained by currently available data, is ≲80%. Previous measurements of the spectral index of the synchrotron emission of the jet of Fornax A between 4.9 and 14.9 GHz (Geldzahler & Fomalont 1978, 1984) also showed a steepening of the spectral index moving from the centre to the outer regions of the jets.

Knowing the magnetic field and the break-frequency of the spectral energy distribution from Eq. (11), we estimate the radiative ages of the kpc-core and jets. The kpc-core seems to be currently active and the age of the synchrotron emission is $\sim 1^{+0.3}_{-0.5}$ Myr. By contrast, the jets do not seem to be currently replenished with energetic particles. Their last active phase seems to have occurred $3^{+7}_{-2}$ Myr ago and to have lasted $\lesssim 1^{+6}_{-0.5}$ Myr.

## 6. Spectral index and break-frequency maps

In this section, we use the high-resolution observation from MeerKAT to generate the spectral index map of the radio emission of Fornax A between 1.03 GHz and 1.44 GHz. The continuum images at the two frequencies are convolved to a common Gaussian beam of 10″ × 10″. The spectral index map is computed pixel-by-pixel measuring the intensity ratio between the two images.

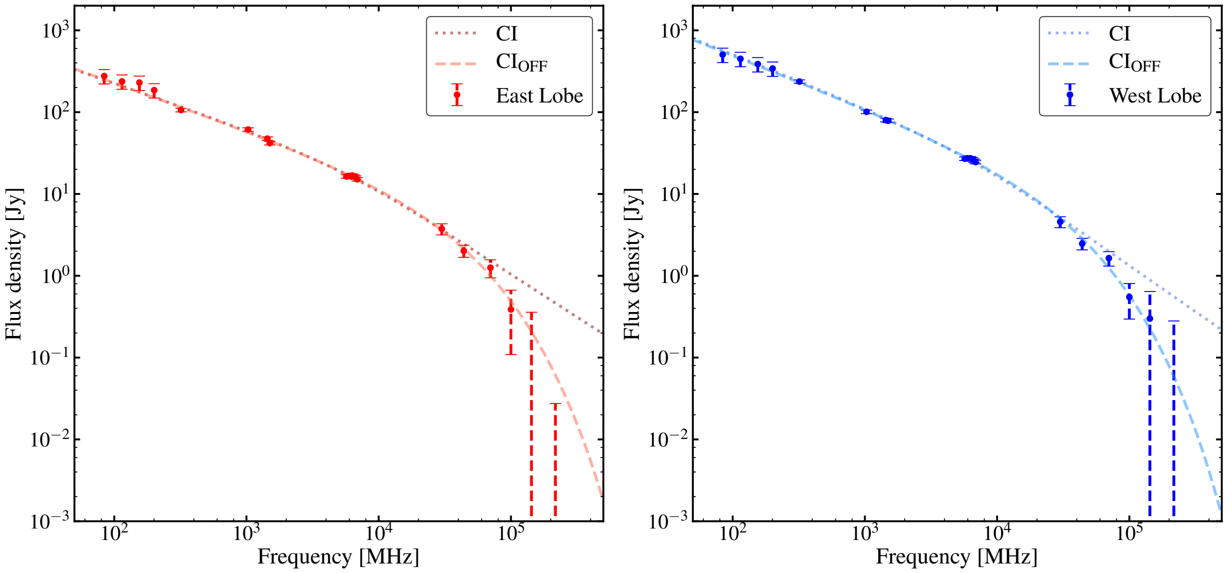


**Fig. 7.** *Left panel*: spectrum of the east lobe fitted with a CI model and a CI with a turn-off ($CI_{OFF}$). *Right panel*: spectrum of the west lobe fitted with the same models as in the left panel.

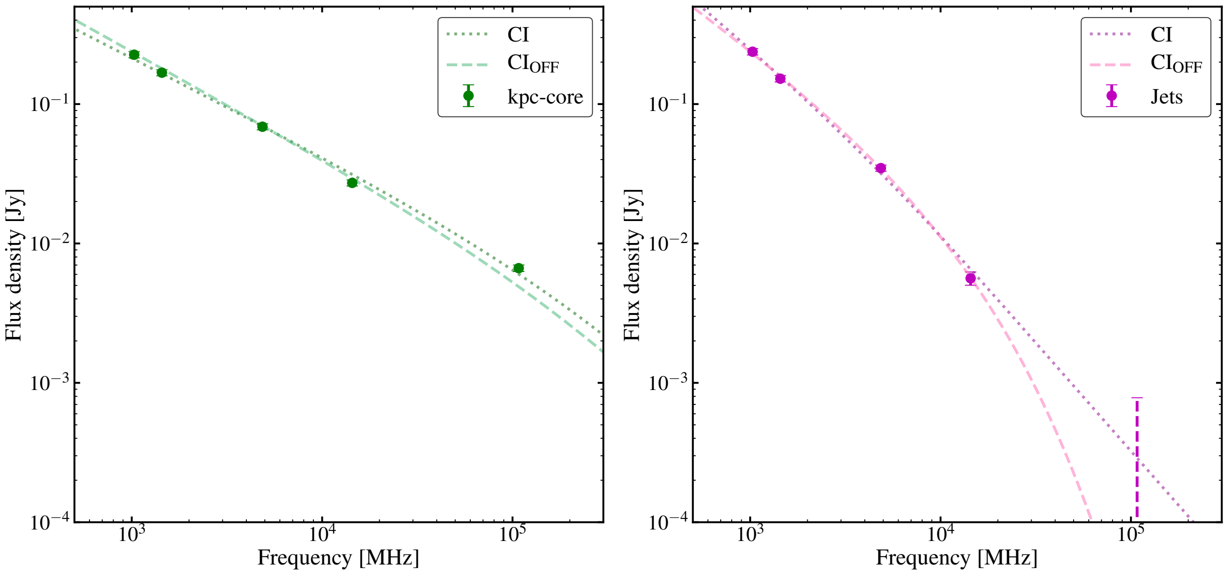


**Fig. 8.** *Left panel*: spectrum of the kpc-core of Fornax A (green) fitted with a CI model and a CI model with a turn-off ($CI_{OFF}$). *Right panel*: spectrum of the extended central radio jets fitted with the same models as in the left panel.

**Table 6.** Physical parameters of the radio emission of the different components of Fornax A according to the results of the spectral modelling.

| Component | $\tilde{\chi}^2$ | | $\alpha_{inj}$ | | $\nu_{break}$ [GHz] | | $t_{OFF}/t_s$ |
|---|---|---|---|---|---|---|---|
| | CI | $CI_{OFF}$ | CI | $CI_{OFF}$ | CI | $CI_{OFF}$ | $CI_{OFF}$ |
| Total | 1.29 | 0.38 | $0.59^{+0.01}_{-0.05}$ | $0.62^{+0.03}_{-0.07}$ | $9^{+2}_{-4}$ | $39^{+4}_{-31}$ | $0.59^{+0.23}_{-0.49}$ |
| East lobe | 1.65 | 1.03 | $0.54^{+0.02}_{-0.06}$ | $0.57^{+0.02}_{-0.10}$ | $8^{+2}_{-4}$ | $32^{+8}_{-27}$ | $0.49^{+0.08}_{-0.42}$ |
| West lobe | 1.80 | 0.45 | $0.63^{+0.02}_{-0.04}$ | $0.63^{+0.02}_{-0.04}$ | $9^{+2}_{-3}$ | $33^{+9}_{-26}$ | $0.53^{+0.18}_{-0.41}$ |
| kpc-core | 10.1 | 20.3 | $0.67^{+0.02}_{-0.03}$ | $0.68^{+0.02}_{-0.03}$ | $\gtrsim 250$ | $\gtrsim 250$ | – |
| Jets | 2.69 | 1.01 | $1.05^{+0.06}_{-0.16}$ | $0.92^{+0.09}_{-0.20}$ | $7^{+2}_{-5}$ | $19^{+2}_{-16}$ | $0.89^{+0.01}_{-0.71}$ |

**Notes.** $\tilde{\chi}^2$: reliability of the best-fit model. $\alpha_{inj}$: injection index of the flux density distribution. $\nu_{break}$: break-frequency of the spectrum. $t_{OFF}/t_s$: ratio between the total lifetime of the AGN and the off-phase. Further details about these parameters are given in Sect. 5.